Research paper

Determination of bi-dimensional normal residual stress distributions in metallic laser-based powder bed fusion parts

Joaquin Montero [a,b], Sebastian Weber [a,b,*], Matthias Bleckmann [b], Kristin Paetzold [c], Eric A. Jägle [a]

[a] *Universität der Bundeswehr München, Werner-Heisenberg-Weg 39, Neubiberg, Germany*
[b] *Bundeswehr Research Institute for Materials, Fuels and Lubricants (WIWeB), Institutsweg 1, Erding, Germany*
[c] *Technische Universität Dresden, Institute of Machine Elements and Machine Design, George-Bähr-Straße 3c, Dresden, Germany*

ARTICLE INFO

ABSTRACT

Disadvantageous complex residual stress distributions are common in parts manufactured by laser-based powder bed fusion metals (PBF-LB/M). Thus, the residual stress state determination is essential for understanding the part's limitations. One residual stress measurement technique applicable to PBF-LB/M parts is the slitting method. This destructive technique allows through-thickness measurements and copes well with discontinuities in the material, yet is limited to one-dimensional stress profiles. Conversely, other stress measurement techniques, e.g. X-ray diffraction, are restricted to the part's surface. This article presents an inexpensive and straightforward stress determination approach that combines an implementation of the slitting method with X-ray diffraction measurements to create a continuous two-dimensional residual stress map along a part's cross-section. The approach was numerically validated using finite element models that simulate, on the one hand, the PBF-LB/M process and, on the other hand, the measuring process; further, it was experimentally tested in PBF-LB/M AlSi10Mg samples. The use of linear elastic fracture mechanics allowed a straightforward formulation of the approach, which enabled a high degree of automation. The accurate stress distribution results and the correlation with the simulations and previous studies demonstrate the approach's robustness and effectiveness for complex residual stress states determination in two dimensions.

1. Introduction

In recent years, there has been increasing interest in metal additive manufacturing (AM) or metal 3D Printing. It has become an established industrial manufacturing technology, while emerging as the fastest-growing AM market (AMFG, 2020). Powder bed fusion (PBF), one of the seven categories of AM processes (ASTM, 2015), made up 88% of the installed capacity of metal AM technologies by 2020 (Wohlers et al., 2020). Laser-based powder bed fusion of metals (PBF-LB/M) is a subcategory of PBF that uses a laser as energy source to melt metallic powder material in a powder bed selectively (ISO/ASTM, 2019). The PBF-LB/M process has complex thermal characteristics as fast temperature changes occur due to the moving laser spot and the repetitive nature of the process. Thus, large thermal gradients form, caused by the temperature difference between the melt pool and the part, substrate and build-environment. These characteristics lead to local deformations and residual stress (RS) at the micro-structure level and meso-structure level during the build, which later translates into bulk-RS or macro-RS in the finished part (Liu et al., 2016). RS are mitigated by using

support structure, platform preheating and post-processing, yet all of these increase the build cost considerably (Vrancken, 2016).

Pores and other material discontinuities can occur in PBF-LB/M (Yu et al., 2019). Therefore, the presence of tensile RS can trigger the nucleation and propagation of cracks, reducing the part's fatigue life (Danninger and Weiss, 2003). Consequently, being aware of RS states in the manufactured part is of utmost importance in this AM process, even if the part appears to be within geometric tolerance after the build. For that, on the one hand, analytical models (Fergani et al., 2017) and process simulation (Li et al., 2016; Luo and Zhao, 2018) allow us to understand the nature of RS and explain the typical RS distributions in PBF-LB/M parts, like the tensile states in the surface and subsurface of the parts. Yet, with the use of intricate scan strategies as it is common in modern PBF-LB/M systems, the problem difficulty escalates. Nevertheless, recent advances in computational modeling of PBF-LB/M, particularly at the layer scale, show the dynamics of the thermal gradients during melting and solidification and estimate distortions and RS considering the scanning strategy (Zhang et al., 2020).

Nomenclature

$\boldsymbol{\Lambda}$	Segmented weight function tensor
ϵ_{xx}^{M}	Normal strain at the position M in x-direction
ν	Poisson's modulus
σ_n	Normal stress
σ_{xx}	Normal stress in x-direction
σ_{xx}^{mean}	σ_{xx} averaged across the thickness
a	Crack length
E'	Generalized Young's modulus
F	Virtual Force
h	Weight function
K_I	Stress intensity factor, mode I
K_{IF}	Stress intensity factor, mode I, due to F
M	Measuring point
N_i	Orthogonal basis functions
s	Distance between M and application point of F
t	Thickness
U	Strain energy
u_x^M	Displacement at the point M in x-direction
w	Width
Z	Influence function

On the other hand, it is possible to measure RS experimentally, obtaining results regardless of the utilized PBF-LB system configuration. Still, measuring complete RS states in PBF-LB/M parts is often expensive and time-consuming. Among the measurement methods, the most popular in metal AM are X-ray diffraction (XRD) and hole drilling, mainly because of the equipment availability and existing standards (Acevedo et al., 2020). XRD is only suitable for measuring stresses close to the surface, given its low penetration depth. Due to the rough surface of PBF-LB/M parts, XRD measurements often require surface conditioning (Chen et al., 2020). XRD is found to effectively retrieve the macro-stresses acting in the Al-matrix for AlSi10Mg PBF-LB/M specimens (Marola et al., 2021; Vrancken et al., 2013; Rosenthal et al., 2018).

The slitting method, previously known as the crack compliance method (Cheng and Finnie, 2007) is one type of destructive RS measurement techniques. This method determines RS distributions by analyzing the part's deformation, when a slot is incrementally machined out of it, simulating a crack propagation. The slitting method is executed in a similar fashion as the standardized incremental hole drilling method (ASTM, 2020b). It has proven to be an effective solution for stress determination in metal AM parts. Mercelis and Kruth (2006) applied it to PBF-LB/M parts using 316L steel. Strantza et al. (2019) used it in Directed Energy Deposition specimens of Ti6Al4V, achieving remarkable stress results at the meso-scale level. Besides, as a destructive stress determination technique, the slitting method can advantageously be used to determine resultant stresses throughout the parts' thickness. The required strain measurement is performed away from the machining area, which avoids the influence of local plastic deformations. Furthermore, the method is not dependent on surface quality.

RS distributions caused by the PBF-LB/M process are complex and dependent on the part's shape, usually exhibiting peak values on the outer skin. Thus, a new approach for determining two-dimensional RS distributions in a cross-section is developed in this article. The approach targets PBF-LB/M parts, yet, as it is derived from a generic formulation, it applies to any other metallic AM process. For that purpose, an implementation of the slitting method coupled with X-ray diffraction

measurements was proposed and was experimentally applied to PBF-LB/M test specimens. The presented formulation calculates macro-RS and allows a high degree of automation due to the iterative nature of the approach. This way, the user is prevented from performing interpolations that could detriment the quality of the measurement results, allowing for a large number of measurement points without adding significant effort. The approach was validated through several finite element (FE) simulations in ideal and realistic conditions. Additionally, recommendations for successfully applying the method to PBF-LB/M parts are given to encourage researchers to exploit its capabilities and extend it to further use cases.

2. Materials and methods

Although the highest normal RS in PBF-LB/M parts is in the building direction (Shiomi et al., 2004; Mercelis and Kruth, 2006; Vrancken, 2016), an implementation of the slitting method is presented and formulated here for calculating normal RS distributions in the perpendicular direction. This way, the method's capabilities over the less sensitive dimension is tested. The coordinate system is consistent throughout the article with the commonly used coordinates for PBF-LB/M systems. The normal stress in x-direction, σ_{xx}, is selected for the analysis. Nevertheless, the method can be adapted following the same procedure to calculate other components of the stress tensor.

2.1. An implementation of the slitting method

The slitting method was originally introduced by Vaidyanathan and Finnie (1971) as a destructive technique. It is used to determine a one-dimensional residual stress distribution by deliberately creating and propagating a crack in a test specimen (Prime, 1999). There are different ways to formulate the method (Cheng and Finnie, 2007). Still, each one relies on monitoring the specimen's deformation and on calculating an elastic inverse problem. The deformations result from stress relaxation created by the new crack increment. The crack, notch or slot is commonly machined by using electric discharge machining or a thin saw. The deformation can be measured as crack opening displacements or strain at a pre-determined measuring position by using strain gauges.

As a common practice, the slitting method uses a compliance matrix to calculate the RS state from the measured strain (Schajer and Prime, 2006). This matrix is created following a standard approach that requires a prior finite element analysis of the geometry (Hill and Lin, 2002). Series expansion methods are then used to approximate the stress distribution and to solve the elastic inverse problem defined by the compliance matrix and the measured strain (Cheng and Finnie, 2007). This problem is application-specific and depends on the user's experience and expertise to achieve acceptable, use-case specific measurement results. This article uses a simple, yet powerful formulation that relies on Linear Fracture Elastic Mechanics (LFEM) to calculate the Stress Intensity Factor (SIF) K. This result is then used to retrieve the residual stress profile that existed on the created crack plane in the uncracked body (Schindler, 1996).

As test specimen, the rectangular sample appearing in Fig. 1 was analyzed. It is in concordance with the Single Edge Notch test specimen (SEN) from the ASTM E399-20 standards (ASTM, 2020a). Furthermore, this geometry was idealized to 2D and considered under the hypothesis of plane strain, following the work of Aydıner and Prime (2013). They emphasize that for the slitting method, plane strain is the preferred approximation for relatively thick plates.

In this analysis, the crack opening is considered to be perpendicular to the crack, due to a tensile stress normal to the crack plane (opening mode or *Mode I*) (Farahmand, 2001). For this case, the change of strain energy U due to the presence of a crack is given by:

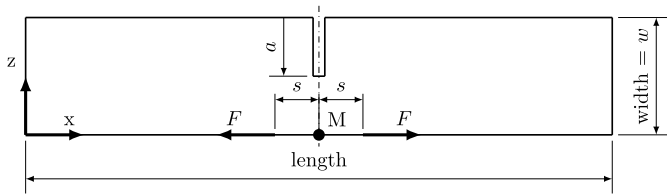$$U(a) = \frac{t}{2E'} \int_{a_0=0}^{a} K_I^2 \, da \tag{1}$$

Fig. 1. 2D representation of the SEN specimen.

where $E' = E$ for plane stress or $E' = E/(1 - \nu^2)$ for plane strain with ν as the Poisson's ratio and E as the Young's modulus. $K_I(a)$ is the SIF in the opening *Mode I* due to a normal stress $\sigma_{xx}(z)$. The thickness is normalized and considered unitary $t = 1$.

To analyze the correlation between the deformation at an arbitrary measuring point M and the energy variation due to the propagation of a crack, opposite virtual forces are introduced in direction of the measurement at a distance s. This is illustrated in Fig. 1.

The change in strain energy U is also a function of the stress intensity factor K_{IF}, which is caused by a virtual force.

$$U(a, s) = \frac{1}{2E'} \int_{a_0=0}^{a} \left(K_I + K_{IF} \right)^2 \, da \tag{2}$$

To obtain the displacement in x-direction at the measuring point M, the Castigliano's theorem is applied, setting the virtual forces to zero.

$$u_x^M(a, s) = \frac{\partial U(a, s)}{\partial F}\bigg|_{F=0} = \frac{1}{2E'} \int_{a_0=0}^{a} \frac{\partial \left(K_I + K_{IF} \right)^2}{\partial F} \, da \tag{3}$$

F is independent from a and the stress intensity factor K_I from the virtual force F. Therefore, $\partial K_I / \partial F$ is equal to zero. Furthermore, K_{IF} is equal to zero as well. Consequently, the expression for the displacement can be written as:

$$u_x^M(a, s) = \frac{1}{E'} \int_{a_0=0}^{a} K_I \frac{\partial K_{IF}}{\partial F}\bigg|_{F=0} \, da \tag{4}$$

To retrieve the expression of the normal strain at the point M, the derivative of the previous expression is taken with respect to s.

$$\varepsilon_{xx}^M = \frac{\partial u_x^M(a, s)}{\partial s} = \frac{1}{E'} \int_{a_0=0}^{a} K_I \frac{\partial^2 K_{IF}}{\partial F \partial s}\bigg|_{F=0} \, da \tag{5}$$

The term $\partial^2 K_{IF} / \partial F \partial s \big|_{F=0}$ is called influence function Z (Schindler et al., 1997). This function is used to calculate SIFs of a crack based on the specimen's deformation. Z depends on the geometry, the crack plane and the strain measuring position M. For the SEN specimen in opening *Mode I* and the measuring position M at the edge below the crack, as shown in Fig. 1, Z is given by (6). The coefficients C_1 through C_3 are -2.532, 5.926 and -0.288 with $s = 0$ and $F = 0$ (Schindler and Bertschinger, 1997). Finally, the strain can be expressed as in (8).

$$Z(a) = \begin{cases} \frac{C_1}{(w-a)^{1.5}} \sqrt{1 - 25\zeta^2} \left[C_2\zeta^2 + C_3\zeta + 1 \right] & \forall \frac{a}{w} < 0.2 \\ \frac{C_1}{(w-a)^{1.5}} & \forall \frac{a}{w} \geq 0.2 \end{cases} \tag{6}$$

$$\zeta = \left(0.2 - \frac{a}{w} \right) \tag{7}$$

$$\varepsilon_{xx}^M = \frac{1}{E'} \int_{a_0=0}^{a} K_I Z(a) \, da \tag{8}$$

K_I is obtained by the derivative of (8) with respect to a.

$$K_I(a) = \frac{E'}{Z(a)} \frac{d\varepsilon}{da}\bigg|_{a} \tag{9}$$

The latter expression is used for the calculation of K_I in this implementation of the slitting method. To relate K_I to the specimen's RS before the crack existed, the weight function $h(z, a)$ is used. This method was initially proposed by Bueckner (1970) and Rice (1972) to determine the SIF in a pre-determined body geometry, independent of the load case. K_I can also be expressed as follows:

$$K_I(a) = \int_{a_0=0}^{a} h(z, a) \cdot \sigma_n(z) \, dz \tag{10}$$

where $\sigma_n(z) = \sigma_{xx}(z)$ is the normal stress distribution along the crack plane in the uncracked body (Glinka and Shen, 1991). The weight function $h(z, a)$ used in this article for the SEN specimen, was developed using the results from Fett (2008) and normalized for a unitary thickness in (11) with λ, m_1 and m_2 according to (12)–(14).

$$h(z, a) = \sqrt{\frac{2}{\pi \cdot a}} \left\{ \lambda^{-0.5} + m_1 \cdot \lambda^{0.5} + m_2 \cdot \lambda^{1.5} \right\} \tag{11}$$

$$\lambda = \lambda(z, a) = 1 - \frac{z}{a} \tag{12}$$

$$m_1 = m_1(a) = 0.6147 + 17.1844 \left(\frac{a}{w} \right)^2 + 8.1822 \left(\frac{a}{w} \right)^6 \tag{13}$$

$$m_2 = m_2(a) = 0.2502 + 3.2889 \left(\frac{a}{w} \right)^2 + 70.0444 \left(\frac{a}{w} \right)^6 \tag{14}$$

To calculate the SIF (10), it is necessary to know the analytical expression of $\sigma_{xx}(z)$. In a simplified way, $\sigma_{xx}(z)$ is considered constant within the crack interval $[a_0, a]$. This is valid as long as the crack increment $|a - a_0|$ is small enough to represent the variations on the stress distribution $\sigma_{xx}(z)$ along the z-coordinate. The generic crack a_i can be defined as the sum of finite crack increments, $a_i = \sum_{j=1}^{i} |a_{j-1} - a_j|$. To each interval $a_{j-1} \leq z \leq a_j$ corresponds a constant value of normal stress σ_{xx}^j with K_I:

$$K_I = \int_{a_0=0}^{a} \sigma_{xx}(z) \, h(z, a) \, da = \sum_{j=1}^{i} \sigma_{xx}^j \int_{a_{j-1}}^{a_j} h(z, a_i) \, dz \tag{15}$$

With (9) leading to the implementation of the slitting method used in this article:

$$\frac{E'}{Z(a_i)} \frac{d\varepsilon_{xx}^M}{da}\bigg|_{a_i} = \sum_{j=1}^{i} \sigma_{xx}^j \int_{a_{j-1}}^{a_j} h(z, a_i) \, dz \tag{16}$$

The above equation represents the linear system of Eqs. (17), in which the components σ_{xx}^j of the vector $\boldsymbol{\sigma_{xx}}$ are unknown. The tensor $\boldsymbol{\Lambda}$ contains the segmented integral of the weight function along the crack plane. A detail to observe is that for the elements in the main diagonal, the weight function becomes singular.

$$\boldsymbol{K_I} = \boldsymbol{\sigma_{xx}} \cdot \boldsymbol{\Lambda} \tag{17}$$

$$\Lambda^{ij} = \begin{cases} \int_{a_{j-1}}^{a_j} h(z, a_i) \, dx & \forall \quad i \geq j \\ 0 & \forall \quad i < j \end{cases} \tag{18}$$

$$K_I^i = \frac{E'}{Z(a_i)} \frac{d\varepsilon_{xx}^M}{da}\bigg|_{a_i} \tag{19}$$

A MATLAB® implementation was developed using the Gauss–Kronrod quadrature integration to deal with the mentioned singularities of the weight function. The five-point-stencil method was used to calculate the strain derivative with the condition that the provided strain data must be equispaced along the propagation axis. Furthermore, it also requires the extrapolation of two strain values beyond the measuring domain. This way, the method's particular implementation does not demand fitting of the measured strain.

2.2. Analysis of a cross-sectional stress distribution

As the implementation of the slitting method is presented for 2D, the hypothesis of no stress variation across the thickness t is adopted, $\partial \sigma_{xx}(z)/\partial y = 0$. Consequently, only an averaged stress state across the thickness $\sigma_{xx}^{mean}(z_i)$ can be retrieved for each cut increment z_i. This is valid, because the strain variation results from the stress relaxation, which is induced by a complete cut along the y-coordinate. If intermediate states along the y-coordinate are pursued, the cut needs to be incremental through the thickness. Thereby, the strain in these

intermediate steps can be queried. This cutting strategy is challenging to achieve by machining, can be very time consuming and would require an excellent sensitivity of the strain data acquisition system.

However, it is possible to infer the rest of the stresses existing in the crack plane, i.e. the cross-section yz, because additionally to $\sigma_{xx}^{mean}(z_i)$, which can be determined by the slitting method, also the stress distribution near the specimen's surface is obtainable by other well-established RS measurement techniques. For this case, orthogonal quadratic basis functions $N_i(y)$ were used to approximate stresses along the thickness profile. This practice is similar to the formulation of the Finite Element Method (Zienkiewicz et al., 2013). Therefore, the stress profile across the thickness can be expressed as in (20), with $\sigma_1 = \sigma_{xx}^{y=0}(z_i)$ and $\sigma_3 = \sigma_{xx}^{y=t}(z_i)$ as the normal stress measurements at the surface. XRD was used to obtain them. The stress $\sigma_2 = \sigma_{xx}^{y=t/2}(z_i)$ is calculated by (21) coupled with the definition of mean stress, using the same orthogonal basis. This is feasible as long as the macro-stress distribution can be approximated by the selected basis. But it can be expanded to higher order approximations, depending on the use-case and the penetration depth of the additional stress measurement method.

$$\sigma_{xx}(y, z_i) = \sum_{j=1}^{3} \sigma_j \, N_j(y) \tag{20}$$

$$\sigma_{xx}^{mean}(z_i) = \frac{1}{t} \int_0^t \sigma_{xx}(y, z_i) \, dy \tag{21}$$

Once $\sigma_{xx}(y, z_i)$ is obtained for the whole measurement domain, it is possible to create interpolations of higher order along the z-axis to create a field $\sigma_{xx}(y, z)$. The interpolation order should be consistent with the number of cutting increments i. Hermite cubic spline interpolations were used to create the 2D macro-RS field in the cross-section.

2.3. Numerical validation of the slitting method for PBF-LB/M samples

To test the presented slitting method implementation, two different FE models were created within the commercial software ANSYS® Workbench™ and ANSYS® Additive Print™. Both simulations act as virtual representation of the cutting process in a pre-stressed body, exhibiting an increasing crack length a and the consequent strain $\varepsilon_{xx}^M(a)$ acquisition. The obtained strain vector ε_{xx}^M was used as an input to the MATLAB® implementation, which is presented in the previous section. The stresses calculated via the slitting method were then compared to the initial stress of each FE model to evaluate the robustness of the implementation.

First, a 2D model idealization was created, following the hypothesis presented in Section 2.1. A few different initial residual stress distributions were investigated within the 2D model. Second, the formulation capabilities were tested in a realistic 3D model using an initial stress distribution given by a simulation of the PBF-LB/M process, also adding measuring noise in the strain vector. The process parameters were in accordance with the experimental use-case presented in Section 2.4. A block diagram of both models is shown in Fig. 2.

2.4. Experimental setup

For experimental testing, a total of 5 specimens were produced with a length of 120 mm, width of 20 mm and thickness of 10 mm on a single build plate. An SLM® 280HL PBF-LB/M system was used with the process parameters shown in Table 1, a chess pattern scanning strategy with a rotation of 67°, and a base temperature of 200 °C. The orientation of the specimens on the build platform followed the reference system of Fig. 1, with z as the build direction and y as the recoating direction. SLM® AlSi10Mg powder was used as raw material with a particle size volume distribution of D10 = 27.9 μm D50 = 42.4 μm and D90 = 59.7 μm, and a mean diameter D[4,3] = 43.4 μm.

The creation and propagation of the notch was performed via an automated setup, consisting of a CNC milling machine and a data
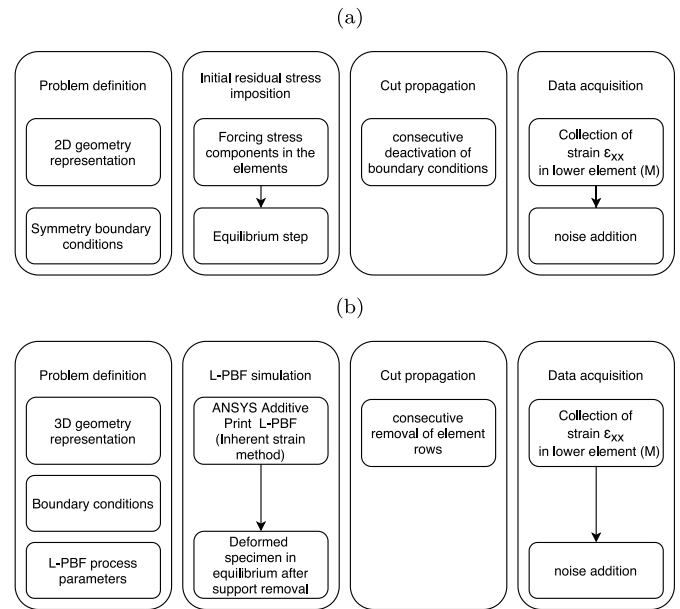

Fig. 2. Block diagram for the proposed slitting method simulations in 2D (a) and 3D (b).

Table 1
Machine parameters of the SLM 250HL PBF-LB/M system.

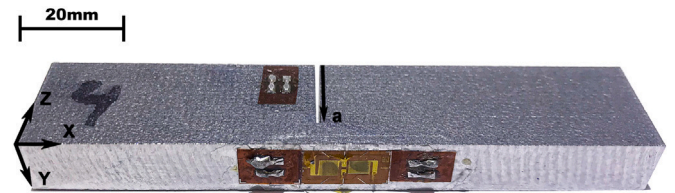| Laser power	Scan speed	Layer thickness	Hatch spacing	Hatch width	Beam diameter
350 W	1150 mm s^{-1}	50 μm	120 μm	10 mm	80 μm

Fig. 3. AlSi10Mg PBF-LB/M specimen after cutting operation.

acquisition system. The cutting was performed along the y-direction. An HSS circular saw with a diameter of 80 mm and a thickness of 0.25 mm was used, rotating at 300 min^{-1}. The cutting speed was 40 mm min^{-1} in y-direction and 0.05 mm per cut in z-direction. Such slow cutting speeds were set to avoid possible machining induced stresses. The part was clamped on one side of the specimen, far away from the measuring point M, as suggested by Prime (2003). Only 75 % of the geometry was cut, resulting in a total of 300 cuts per test specimen. This number is notably higher than the minimum number of cuts recommended by Prime and Hill (2006), in order to capture finer stress variations. One of the specimens after the cutting process is shown in Fig. 3.

To measure the strain, a strain gauge HBM® XY11-3/120 was used. The strain data was acquired using a National Instruments™ DAQ NI-9237 interface and the National Instruments™ Labview software. The excitation voltage was 5 V at a sample rate of 10 kHz. The sampling signal was compressed using mean reduction with a factor of 100. The strain measurement was systematically taken 2 s after each cut operation.

To measure RS next to the part's surface and further verify results, an X-ray diffractometer Bruker™ D8 Discover with a CuKα radiation source was used at 40 kV and 40 mA. The implemented method was $\sin^2 \psi$, at diffraction angles 2θ from 135° to 141° corresponding to the
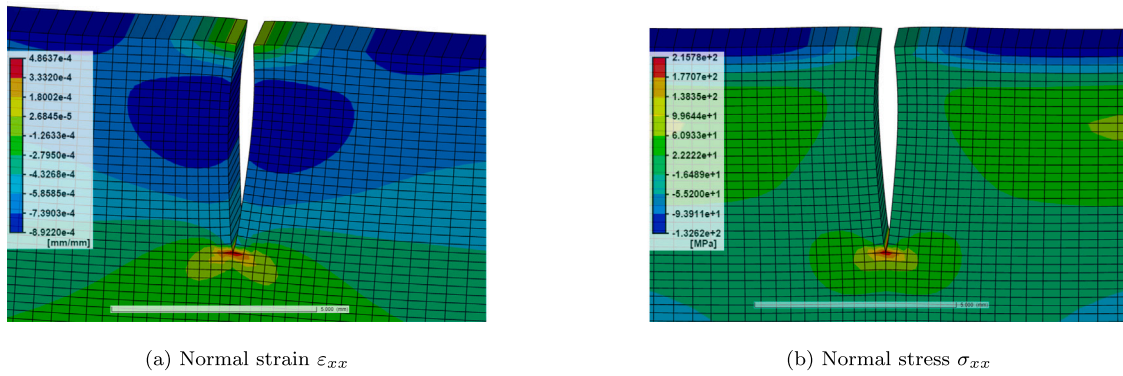
(a) Normal strain ε_{xx}

(b) Normal stress σ_{xx}

Fig. 4. Rendering of the 2D idealization model, displaying results for 5 mm crack length. Displacements are scaled by a factor of 100. The stress distribution correlates to Fig. 5a.

{311} aluminum reflex, following the recommendations from Marola et al. (2021). A 20 μm Ni filter was used to filter Cu-Kβ radiation and a soller slit of 2.5° was set on both source and detector side, as well as a snout collimator of 1 mm diameter to measure macro-RS. The specimen's surface was ground up to 2000 grit and polished down to a 1 μm surface finish before the measurements to diminish surface roughness induced errors. The Poisson's ratio was set to $v = 0.33$ and the Young's modulus to $E = 68$ GPa, accordingly to properties of PBF-LB/M AlSi10Mg perpendicular to the build direction (Kempen et al., 2012).

3. Results

3.1. Test on 2D simulation data

The 2D FE model was a symmetric representation that used elements of the type *PLANE182* with a linear element approach function. Full integration and enhanced strain formulation was used to prevent shear locking. The geometry was in concordance with the dimensions given in Section 2.4. The mesh was structured with a consistent size of 0.2 mm in *y*-direction and element bias from 0.2 mm to 2 mm along the *x*-direction with the smallest elements next to the crack. Element skewness was prevented by surface meshing.

Three arbitrary initial stress distributions in the range of -100 MPa to 100 MPa were mapped across the part domain. The boundary conditions of the model were a fixed support on the lowest node at the symmetry *z*-axis and symmetric support along the symmetry *z*-axis. The simulation consisted of 100 sub-steps, from which the first one was used to calculate the equilibrium state. Subsequently from the second step on, all degrees of freedom were set free progressively along the symmetry axis parallel to the *z*-axis, emulating a mathematical crack growth. At the end of the simulation, this removal of boundary conditions led to a crack length that reached through the part along the *y*-axis and stopped right before the last element. Fig. 4 shows an example for the strain 4(a) and stress 4(b) distribution for one of the load cases with a 5 mm crack.

The total strain of the lowest element at the symmetry axis along the crack (representing the measuring position M) was exported for each cut propagation. It was then used as an input file for the MATLAB® implementation of the method. The obtained residual stress profile was compared to the initial residual stress state that the FE model had before the first cut propagation. In Fig. 5, the slitting method's stress result is compared to the initial FE stress for three different aleatory exemplary cases. As it can be seen, the slitting method retrieved stresses accurately until approximately 70 % of the cutting length in the worst case.

Calculations of intermediate stress states during the notch propagation can be achieved with $a_0 \neq 0$ in (17). In other words, stress re-distributions can also be computed using the slitting method. Fig. 6

shows exemplary results for different starting notch lengths a_0 for the stress profile of Fig. 5b.

To check that the results obtained are effectively residual stress distributions, each profile was verified to be in force and momentum equilibrium accordingly to (22) and (23). The integral results delivered negative values close to zero, due to the incapacity of the method to retrieve tensile stresses at the end of the geometry, out of the interval of confidence.

$$\int_0^w \sigma_{xx}(z)\, \mathrm{d}z = 0 \tag{22}$$

$$\int_0^w \sigma_{xx}(z)\, z\, \mathrm{d}z = 0 \tag{23}$$

3.2. Test on 3D simulation data

The 3D simulation was split into two separate simulations. First, the PBF-LB/M process was simulated using a thermal strain simulation in ANSYS® Additive Print™. Simulation parameters were set in accordance with the machine parameters, see Table 1. Additionally, machine-dependent strain scaling factors were determined following the ANSYS® guidelines. The strain scaling factor (SSF) and anisotropic strain coefficients (ASC) were experimentally calibrated and are SSF = 0.524, $ASC_{\parallel} = 1.142$ and $ASC_{\perp} = 0.858$. As material, AlSi10Mg with a J2 plasticity stress mode was selected. The simulation used *SOLID185* Cartesian elements with a size of 0.5 mm. The model was then transferred to ANSYS® Mechanical™ for further processing steps. The geometry is supported by a fixed boundary condition on the left side of the sample. A total of 41 load steps were necessary to set the initial conditions, remove the support structure and perform the simulation of the cuts. These cuts are necessary for the implementation of the slitting method. For the simulation of the cutting process, rows of elements at the center of the part were consecutively removed by element death, starting from the top until one row of elements remained. Removing elements by element death represents a realistic slot creation, instead of a mathematical crack.

The total strain was obtained as average strain of the elements covering the area, where the strain gauge was located at the measuring position M. To check the model's sensitivity to measurement noise, Zero-mean Gaussian noise with a variance of $\pm 3\ \mu\varepsilon$ was added to the ε_{xx} vector. Signal conditioning was performed using a Savitzky–Golay filter (Savitzky and Golay, 1964) of third order and a frame length of 11 data points.

The presented formulation of the slitting method retrieves $\sigma_{xx}^{mean}(z_i)$, yet a variation of $\sigma_{xx}(z)$ across the thickness is expected as it has been reported for other AlSi10Mg PBF-LB/M specimens (Salmi et al., 2017). Fig. 7 shows the stress $\sigma_{xx}^{mean}(z)$ averaged across the *y*-direction, taken from the FE model after the PBF-LB/M process simulation. It is compared to $\sigma_{xx}(z)$ that was retrieved by the cutting simulation and implementation of the slitting method.
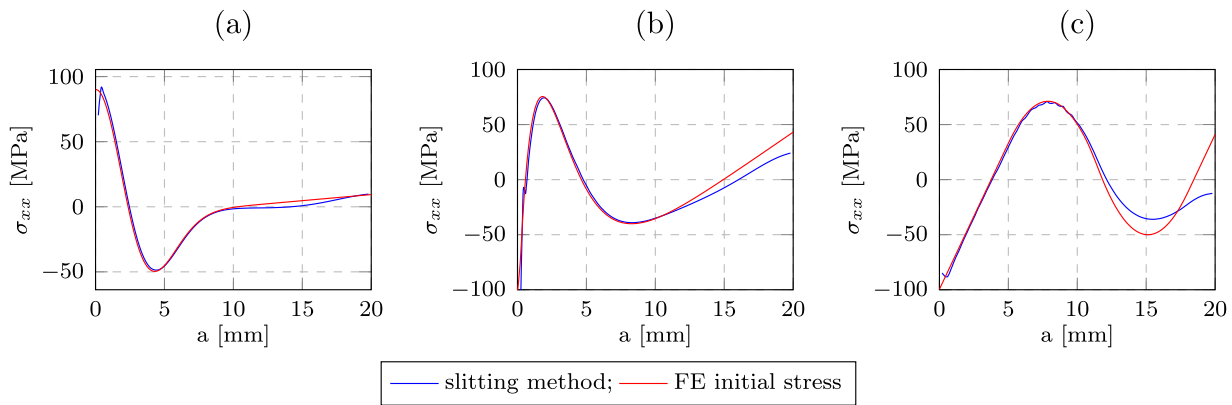
Fig. 5. Comparison of FE initial stress with slitting method calculated stress for three arbitrarily chosen stress distributions (a, b, c).
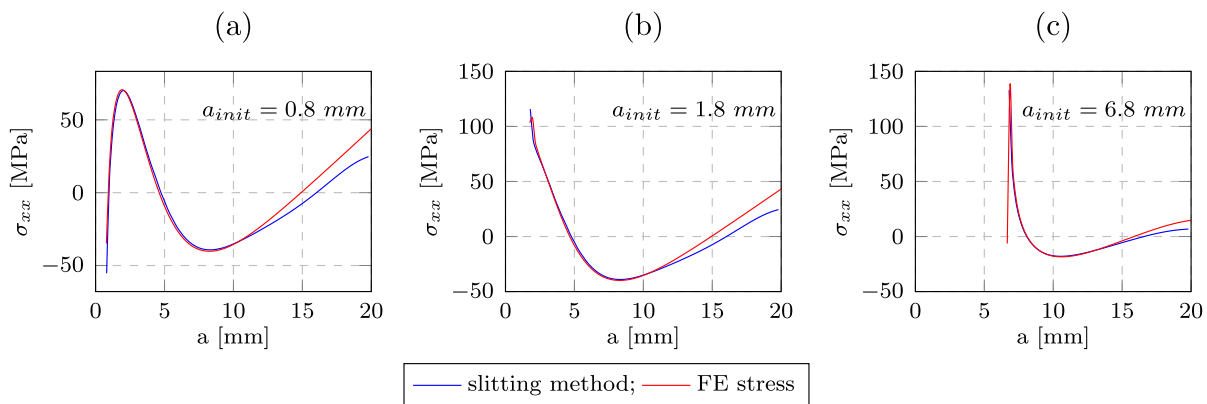

Fig. 6. Comparison of FE stress re-distributions for different initial crack lengths a and slitting method calculated stress profile. Initial crack lengths $0.8\,\mathrm{mm}$ for (a), $1.8\,\mathrm{mm}$ for (b) and $6.8\,\mathrm{mm}$ for (c).
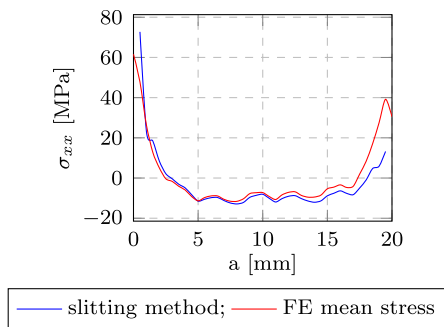

Fig. 7. Comparison of FE initial stress with slitting method calculated stress in the 3D PBF-LB/M simulation model.

To get a deeper understanding about the residual stress distribution along the yz-cross-section, the analysis of Section 2.2 was carried out. Therefore, the RS profile on the specimens' surface was extracted from the FE models. This emulates the obtainment of macro-stresses via some other surface stress measuring technique, e.g. XRD. Then, the stress distributions $\sigma_{xx}^{y=0}(z)$ and $\sigma_{xx}^{y=10}(z)$ were queried from elements on each side of the FE model surface and random noise of $\pm 3\%$ is added. With $\sigma_{xx}^{y=0}(z)$, $\sigma_{xx}^{y=10}(z)$ and $\sigma_{xx}^{mean}(z)$ it is possible to infer the stress distribution field $\sigma_{xx}(y, z)$. The approximation in y-direction was performed using quadratic basis functions. Consequently, it was used to create query points and to plot a 2D stress field by using piecewise cubic hermite interpolation. The resulting field can be seen in Fig. 8(b). The measuring domain is restricted in z, because the stresses in that direction are retrieved by each cut increment z_i. In this case, the cutting

domain was $0.5\,\mathrm{mm}$ to $19.5\,\mathrm{mm}$. A comparison with the initial stress distribution from the FE model can be found in Fig. 8.

The measurement approach results are very close to the FE model stress distribution in the cross-section before the cut propagation. Some waviness can be recognized in the calculated field that follows the initial stress distribution. Similarly, necking of the compressive stress field at $z = 10\,\mathrm{mm}$ was well represented by the slitting-XRD approach simulation. The latter proves a sufficient measuring resolution, even with relatively large cutting increments.

The maximum stress was retrieved within a 10% error margin in the first cut propagation's critical area. Then the compressive stress area is accurately reported together with the transition tensile–compressive stress zone. The minimum stress at the specimen's center shows a discrepancy of around 4 MPa. As expected from the results in Figs. 5, 6 and 7, the stress result accuracy decreases with increasing cutting length. This results in inaccurate values for the stress field's interpolation next to the base of the specimen.

3.3. Experimental test on PBF-LB/M samples

The slitting method was applied to five PBF-LB/M printed specimens. This implementation used the strain derivative over filtered strain data as input. Therefore, there is no error contribution by zero-shift on the strain measurement. Due to the favorable results exhibited in Fig. 7, the stress uncertainties are not reported. Instead, a confidence interval was considered, starting with the third cut propagation until 70% of the specimen's width. The confidence interval was taken from the results shown in Figs. 5 and 7 for a confidence level of 97%.

The unaltered filtering operation, performed in Section 3.2 for the strain measurements, was applied for each test specimen. The results
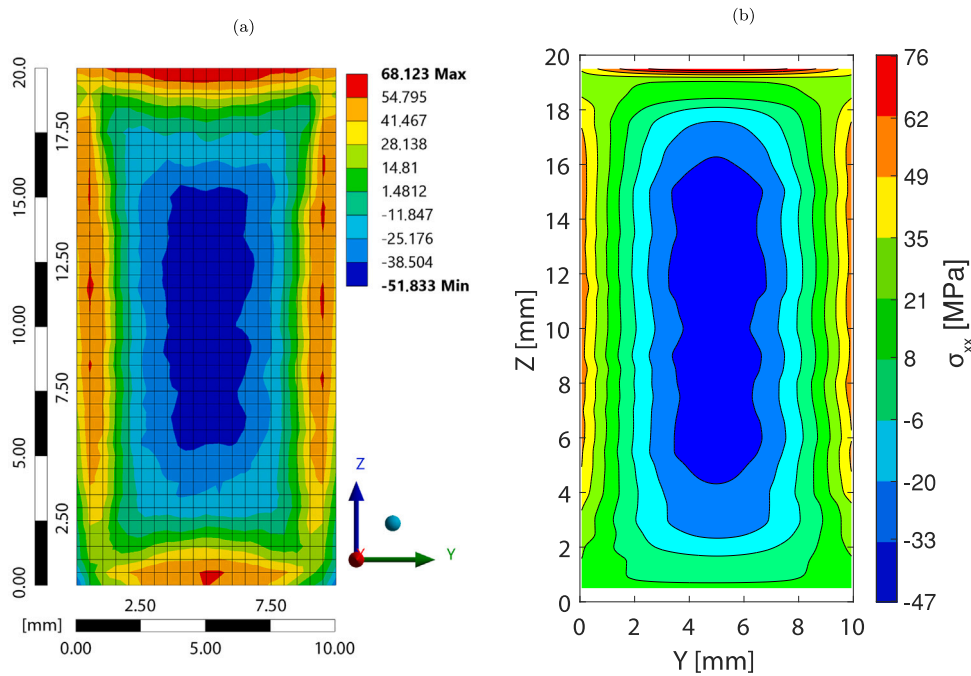
(a)

(b)

Fig. 8. Comparison of FE stress results (a) and results obtained by the proposed approach (b) in the 3D model, for a cross-section at $x = 60\,\text{mm}$.
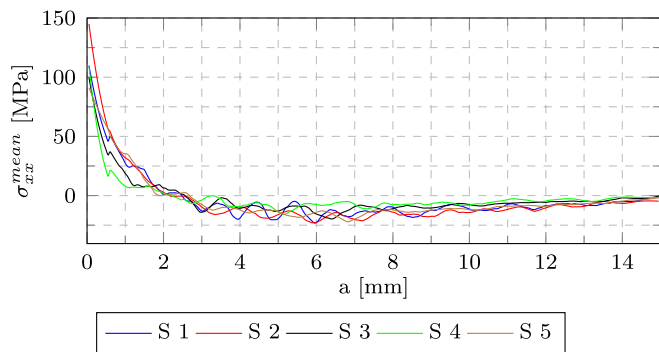

Fig. 9. Mean stress across the thickness via the experimental slitting method in PBF-LB/M specimens S1, S2, S3, S4 and S5.

are reported as a plot in Fig. 9 for a slitting cross-section at $x = 60\,\text{mm}$. In general terms, tensile stress can be observed at the top of the specimens, away form the build platform. From $2\,\text{mm}$ on, compressive stress is dominant across the specimen domain, to counterbalance the tensile stresses next to the part's surface. Some waviness can also be observed in the $4\,\text{mm}$ to $8\,\text{mm}$ zone, which is a possible effect of the stress variations at the meso-scale level, as reported by Strantza et al. (2019).

Qualitatively, the measured stress distribution shares similarities with the stress profile of the FEM simulation, where the shift from tensile to compressive stress is at $a = 3\,\text{mm}$. The maximum measured tensile stress was $145\,\text{MPa}$ for the test specimen S2. The other specimens showed peak values at around $100\,\text{MPa}$. These values are expected to be overestimated, because the method is less precise for the first two values, as it was shown in Fig. 7. This puts the simulation stress values closer to the experimental ones.

The normal stress on the surface was measured via XRD at $y = 0.02\,\text{mm}$ and $y = 9.98\,\text{mm}$. The results are reported $0.02\,\text{mm}$ under the surface to avoid detriment of the measurement due to surface roughness and to be consistent with the XRD penetration depth in aluminum alloys (Tsai et al., 1981; Mercelis and Kruth, 2006; Chen et al., 2020).

The measurements are performed in the range of $1\,\text{mm}$ to $10\,\text{mm}$ in z-direction for every millimeter, due to the diffractor capabilities and the reliable measuring domain of the slitting method. The results were reported for three test specimens in Fig. 10, although all five showed similar results. Tensile stress can be observed in the whole domain of the measurement in the range of $70\,\text{MPa}$ to $150\,\text{MPa}$.

To obtain the bi-dimensional normal stress distribution, the analogue to the previous section was performed. The measurement domain was restricted by the XRD measurements, starting at $z = 19\,\text{mm}$ and finishing at $z = 10\,\text{mm}$. The domain matched the confidence interval of the slitting method measurements.

Tensile normal stresses were evidenced next to the surface, i.e., on the part skin, as it reveals the XRD measurement in Fig. 10, showing peaks of $150\,\text{MPa}$. Given the compressive mean stresses obtained in the bulk, a reversion of σ_{xx} is expected. The calculated $\sigma_{xx}(y, z)$ field for the cross-sectional domain is presented in Fig. 11. As it can be seen, there is a compressive area towards the center of the part, showing valleys of $-100\,\text{MPa}$. These results are qualitatively in accordance with the FE simulation of the PBF-LB/M process, presented in Fig. 8. The values are comparable with the results from Mercelis and Kruth (2006), Vrancken (2016), and Salmi et al. (2017), which obtained similar uni-dimensional profiles for the bulk and surface normal RS for AlSi10Mg in different PBF-LB/M system configurations.

4. Discussion

Regarding the results of the 2D model presented in Fig. 5, there is an initial inaccuracy at the beginning of each plot due to the significant variation in the strain derivative after the first crack propagation. This variation occurs, because the five-point-stencil method needs two additional values beyond the cutting domain, which are extrapolated from the strain curve, to compute said derivative. Moreover, a divergence was observed after 70% of the crack length. This results from the incapacity of the weight function $h(z, a)$ to represent K_1, when the notch length a approaches the total part width. Nevertheless, good accuracy was achieved as the retrieved values do not differ more than 3% from the FEM model values within that interval of confidence. For the stress re-distributions in Fig. 6, a deviation in the results is evident starting after approximately half of the sample width. The behavior
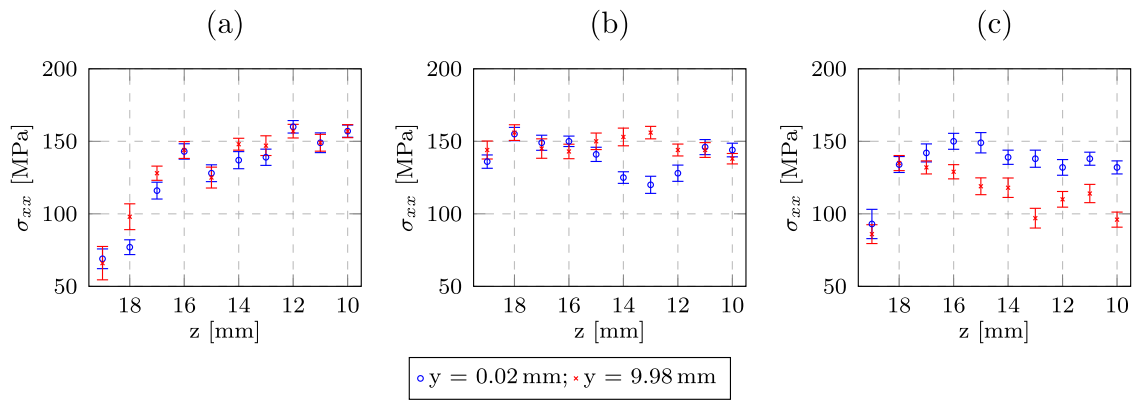
Fig. 10. XRD measurements of normal residual stress at the part's surface, for $x = 60\,\text{mm}$. Specimen S1 in (a), S2 in (b) and S3 in (c). Note that $z = 20$ represents the upper edge of the specimen.
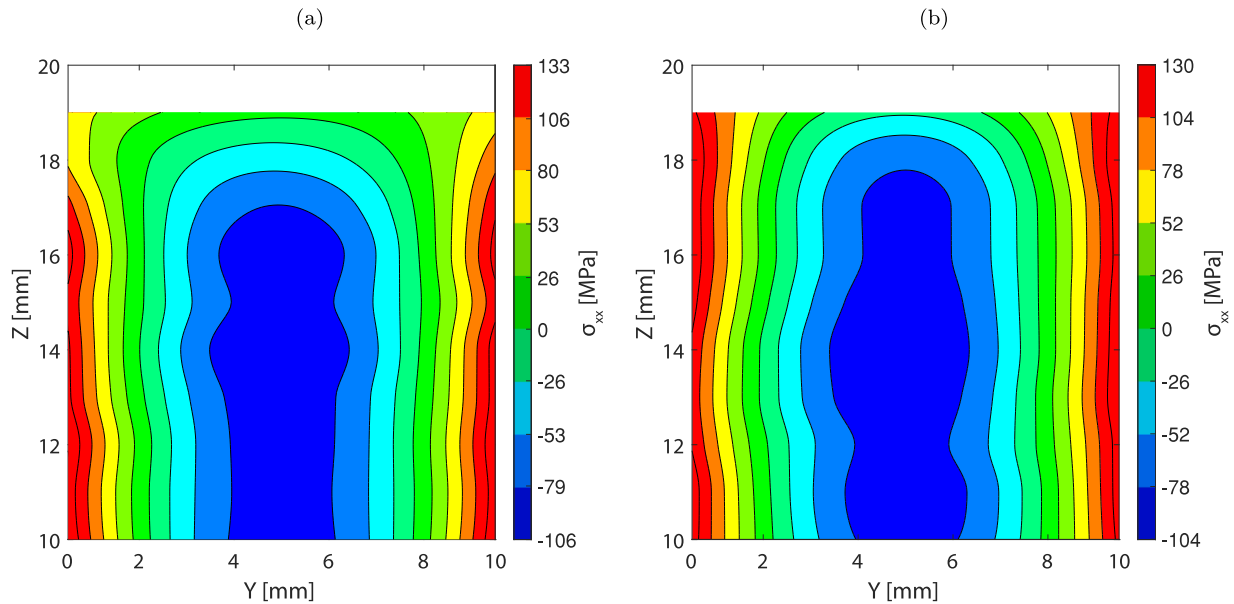

Fig. 11. Results of the 2D normal stress distribution across the thickness for specimens S1 in (a) and S2 in (b).

was similar for different crack lengths. Further, in all the cases, the first cut propagation delivers an inaccurate result, but is immediately followed by a section of good compliance. This is due to the function $h(z, a)$ reaching infinite values for $x/a \approx 1$ and the poor approximation of the derivative at that point. The equilibria of force and momentum delivered small negative values close to zero. These values are not exactly zero due to the induced error of stress values, which are out of the confidence interval, retrieved for large crack lengths.

The 3D implementation shows a similar behavior as the 2D idealization, despite the relatively large cut increment of $0.5\,\text{mm}$, plasticity of the material and the addition of noise. Model errors existed beyond the strain-induced measurement errors. On the one hand, a similar error as in the 2D simulation was present due to the initial derivative approximation. On the other hand, the largest error source was present at the initial crack increment, because the formulation supposes a mathematical crack with non-existent slot width. In this case, the slot width to length ratio was 1:1 for the first cut. Consequently, the largest discrepancy can be observed in the first retrieved stress value, but rapidly converges to the FE model stress from the second value on, which demonstrates the robustness of this implementation. In addition, although the simulation consists of an elasto-plastic model, it is evident that the errors induced by plasticity are negligible in the stress result, as it was demonstrated by Prime (2010). This is because the majority

of the plasticity errors result from yielding that occurs in the crack tip. This yielding is small for the relatively large thickness of the specimen.

The quadratic interpolation along the *y*-axis of the 3D model worked well for this use-case. Nevertheless, the interpolation results in higher stresses next to the surface compared to the original stress of the FE model. These high stresses are present $0.5\,\text{mm}$ under the surface, after the first crack increment. If additional points can be obtained further from the surface, this issue could be solved by using a higher-order interpolation. In practice, this implies the use of a RS measuring method with higher penetration depth than XRD.

The measurements on the experimental setup are in accordance with other studies, reported for PBF-LB/M of AlSi10Mg without post-processing (Mercelis and Kruth, 2006; Salmi and Atzeni, 2017; Wu et al., 2017). Regarding the position of the samples on the build plate, distributions with higher stress values were found for samples located away from the center, which is in accordance with Casavola et al. (2009). The waviness observed in Fig. 11 was an expected result, considering that the cut increment was comparable to the PBF-LB/M process layer height. Therefore, some stresses are reported at the layer interface and some from the intra-layer across the *z*-axis. The use of a smaller cut increment would allow to measure stress variations across the layer, but is impractical for the PBF-LB/M process, as the layer height is typically under $50\,\mu\text{m}$.

Overall, this research article complements the works from Mercelis and Kruth (2006), Williams et al. (2018), Strantza et al. (2019) and Johnson et al. (2019). These researchers applied the slitting method and other RS measurement techniques to AM components, obtaining one dimensional stress profiles. Further, the experimental slitting method of the presented approach was performed in an automated setup with 300 equal cut increments per specimen, a larger number of cut increments than the maximum yet reported (Strantza et al., 2019).

5. Summary and conclusion

This article presented a new approach that determines 2D cross-sectional RS distributions by combining an implementation of the slitting method with XRD stress measurements. It focused on PBF-LB/M parts. Still, it is applicable to any other metallic AM process. With the presented approach, it is possible to obtain complex RS distributions at the complete part depth with simple calculations, which is advantageous compared to other RS measurement methods. Moreover, it is not influenced by discontinuities in the material, such as pores. The approach was validated in a virtual environment via different FE simulations and experimentally in AlSi10Mg PBF-LB/M specimens. The FE models included ideal and realistic unfavorable strain measuring situations, considering plasticity effects, large cut increments and complex initial RS states. Despite the disadvantageous conditions, the approach retrieved good RS approximations, demonstrating its robustness and accuracy.

The experimental measurements retrieved normal RS σ_{xx} distributions perpendicular to the build direction along the whole cross-section of the samples. The specimens showed tensile RS of 70 MPa to 150 MPa in the skin and compressive RS of around 100 Mpa in the bulk of the sample, which is in line with other studies that used other measurement methods (Mercelis and Kruth, 2006; Salmi and Atzeni, 2017; Wu et al., 2017). The location of the tensile–compressive transition zone and the stress peak values correlated to a good extent with FE process simulations. Each retrieved profile was in force and momentum equilibria.

For the automation of the method, we suggest using the five-point-stencil method to calculate the strain first derivative. Also, we recommended using Savitsky–Golay signal filtering on the strain input data for noise reduction. It proved to be an efficient way to minimize noise-induced error in the strain derivative, translating into smoother stress results. The approach's error is only considerable at the very first cut propagation and after a cutting length of 70% of the specimen's width.

This work sets the base for the automation of the method and shows the potential of LFEM for an inexpensive and efficient stress determination in PBF-LB/M specimens. Although only normal stresses were determined, the method can still be expanded to obtain different components of the stress tensor. It can be achieved by adapting the approach, i.e. adjusting the weight and influence functions. Future work may consider extending the approach to different geometries and developing new influence and weight functions.

CRediT authorship contribution statement

Joaquin Montero: Conceptualization, Methodology, Investigation, Formal analysis, Writing – original draft. **Sebastian Weber:** Formal analysis, Visualization, Writing – original draft. **Matthias Bleckmann:** Writing – review & editing , Supervision. **Kristin Paetzold:** Supervision. **Eric A. Jägle:** Writing – review & editing.

Declaration of competing interest

The authors declare that they have no known competing financial interests or personal relationships that could have appeared to influence the work reported in this paper.

Data availability

The raw data required to reproduce these findings as well as the processed data is available upon request.

References

Acevedo, R., Sedlak, P., Kolman, R., Fredel, M., 2020. Residual stress analysis of additive manufacturing of metallic parts using ultrasonic waves: State of the art review. J. Mater. Res. Technol. 9 (4), 9457–9477. http://dx.doi.org/10.1016/j.jmrt.2020.05.092, URL: https://linkinghub.elsevier.com/retrieve/pii/S2238785420313600.

AMFG, 2020. The Additive Manufacturing Landscape 2020. Technical Report, AMFG Autonomous Manufacturing, London, URL: https://amfg.ai/whitepapers/the-additive-manufacturing-landscape-2020-report/#.

ASTM, ISO, 2015. ASTM52900-15 Standard Terminology for Additive Manufacturing—General Principles—Terminology. ASTM International, West Conshohocken, PA.

ASTM, 2020a. E399-20 Test Method for Linear-Elastic Plane-Strain Fracture Toughness KIc of Metallic Materials. Technical Report, ASTM International, E08 Committee, http://dx.doi.org/10.1520/E0399-20, URL: http://www.astm.org/cgi-bin/resolver.cgi?E399-20.

ASTM, 2020b. Test Method for Determining Residual Stresses by the Hole-Drilling Strain-Gage Method. Technical Report, ASTM International E28 Committe, West Conshohocken, PA, http://dx.doi.org/10.1520/E0837-20, URL: https://www.astm.org/Standards/E837.

Aydıner, C.C., Prime, M.B., 2013. Three-dimensional constraint effects on the slitting method for measuring residual stress. J. Eng. Mater. Technol. 135 (3), 031006. http://dx.doi.org/10.1115/1.4023849, URL: https://asmedigitalcollection.asme.org/materialstechnology/article/doi/10.1115/1.4023849/372121/ThreeDimensional-Constraint-Effects-on-the.

Bueckner, H.F., 1970. Novel principle for the computation of stress intensity factors. Z. Angew. Math. Mech. 50 (9).

Casavola, C., Campanelli, S.L., Pappalettere, C., 2009. Preliminary investigation on distribution of residual stress generated by the selective laser melting process. J. Strain Anal. Eng. Des. 44 (1), 93–104. http://dx.doi.org/10.1243/03093247JSA464, Publisher: SAGE Publications Sage UK: London, England.

Chen, Y., Sun, H., Li, Z., Wu, Y., Xiao, Y., Chen, Z., Zhong, S., Wang, H., 2020. Strategy of residual stress determination on selective laser melted al alloy using XRD. Materials 13 (2), 451. http://dx.doi.org/10.3390/ma13020451, URL: https://www.mdpi.com/1996-1944/13/2/451.

Cheng, W., Finnie, I., 2007. Residual Stress Measurement and the Slitting Method. In: Mechanical Engineering Series, Springer US, Boston, MA, http://dx.doi.org/10.1007/978-0-387-39030-7, URL: http://link.springer.com/10.1007/978-0-387-39030-7.

Danninger, H., Weiss, B., 2003. The influence of defects on high cycle fatigue of metallic materials. J. Mater Process. Technol. 143–144, 179–184. http://dx.doi.org/10.1016/S0924-0136(03)00409-6, URL: https://linkinghub.elsevier.com/retrieve/pii/S0924013603004096.

Farahmand, B., 2001. Fracture Mechanics of Metals, Composites, Welds, and Bolted Joints: Application of LEFM, EPFM, and FMDM Theory. Kluwer Academic Publishers, Boston, http://dx.doi.org/10.1007/978-1-4615-1585-2.

Fergani, O., Berto, F., Welo, T., Liang, S.Y., 2017. Analytical modelling of residual stress in additive manufacturing. Fatigue & fracture of engineering materials & structures. Fatigue Fract. Eng. Mater. Struct. 40 (6), 971–978. http://dx.doi.org/10.1111/ffe.12560, URL: https://onlinelibrary.wiley.com/doi/10.1111/ffe.12560.

Fett, T., 2008. Stress Intensity Factors - T-Stresses - Weight Functions. In: IKM, vol. 50, IKM, Karlsruhe, OCLC: 551956131.

Glinka, G., Shen, G., 1991. Universal features of weight functions for cracks in mode I. Eng. Fract. Mech. 40 (6), 1135–1146. http://dx.doi.org/10.1016/0013-7944(91)90177-3, URL: https://linkinghub.elsevier.com/retrieve/pii/0013794491901773.

Hill, M.R., Lin, W.-Y., 2002. Residual stress measurement in a ceramic-metallic graded material. J. Eng. Mater. Technol. 124 (2), 185–191. http://dx.doi.org/10.1115/1.1446073, URL: https://asmedigitalcollection.asme.org/materialstechnology/article/124/2/185/460901/Residual-Stress-Measurement-in-a-CeramicMetallic.

ISO/ASTM, 2019. ISO / ASTM52911 - 1 - 19, Additive Manufacturing - Design - Part 1: Laser-Based Powder Bed Fusion of Metals. Technical Report, ASTM International, West Conshohocken, PA, http://dx.doi.org/10.1520/F3280-19, URL: http://www.astm.org.

Johnson, K., Bishop, J.E., Reu, P.L., Walsh, T., Farias, P.A., Jared, B.H., Susan, D.F., Rouse, J.W., Whetten, S.R., Chen, M.J.Y., Aquino, W., Bellotti, A., Jacobs, L., 2019. Development of a Generalized Residual Stress Inversion Technique. Technical Report SAND2019-13712, 1574171, http://dx.doi.org/10.2172/1574171, URL: http://www.osti.gov/servlets/purl/1574171/.

Kempen, K., Thijs, L., Van Humbeeck, J., Kruth, J.-P., 2012. Mechanical properties of AlSi10Mg produced by selective laser melting. Physics Procedia 39, 439–446. http://dx.doi.org/10.1016/j.phpro.2012.10.059, URL: https://linkinghub.elsevier.com/retrieve/pii/S1875389212025862.

Li, C., Liu, J., Guo, Y., 2016. Prediction of residual stress and part distortion in selective laser melting. Procedia CIRP 45, 171–174. http://dx.doi.org/10.1016/j.procir.2016.02.058, URL: http://linkinghub.elsevier.com/retrieve/pii/S2212827116003401.

Liu, Y., Yang, Y., Wang, D., 2016. A study on the residual stress during selective laser melting (SLM) of metallic powder. Int. J. Adv. Manuf. Technol. 87 (1–4), 647–656. http://dx.doi.org/10.1007/s00170-016-8466-y, URL: http://link.springer.com/10.1007/s00170-016-8466-y.

Luo, Z., Zhao, Y., 2018. A survey of finite element analysis of temperature and thermal stress fields in powder bed fusion Additive Manufacturing. Addit. Manuf. 21, 318–332. http://dx.doi.org/10.1016/j.addma.2018.03.022, URL: https://linkinghub.elsevier.com/retrieve/pii/S2214860417301148.

Marola, S., Bosia, S., Veltro, A., Fiore, G., Manfredi, D., Lombardi, M., Amato, G., Baricco, M., Battezzati, L., 2021. Residual stresses in additively manufactured AlSi10Mg: Raman spectroscopy and X-ray diffraction analysis. Mater. Des. 202, 109550. http://dx.doi.org/10.1016/j.matdes.2021.109550, URL: https://linkinghub.elsevier.com/retrieve/pii/S0264127521001039.

Mercelis, P., Kruth, J.-P., 2006. Residual stresses in selective laser sintering and selective laser melting. Rapid Prototyp. J. 12 (5), 254–265. http://dx.doi.org/10.1108/13552540610707013, URL: https://www.emerald.com/insight/content/doi/10.1108/13552540610707013/full/html.

Prime, M.B., 1999. Residual stress measurement by successive extension of a slot: The crack compliance method. Appl. Mech. Rev. 52 (2), 75–96. http://dx.doi.org/10.1115/1.3098926, URL: https://asmedigitalcollection.asme.org/appliedmechanicsreviews/article/52/2/75/401285/Residual-Stress-Measurement-by-Successive.

Prime, M.B., 2003. Experimental Procedure for Crack Compliance (Slitting) Measurements of Residual Stress. Technical Report LA-UR-03-8629, Los Alamos National Laboratory.

Prime, M.B., 2010. Plasticity effects in incremental slitting measurement of residual stresses. Eng. Fract. Mech. 77 (10), 1552–1566. http://dx.doi.org/10.1016/j.engfracmech.2010.04.031, URL: https://linkinghub.elsevier.com/retrieve/pii/S0013794410002171.

Prime, M.B., Hill, M.R., 2006. Uncertainty, model error, and order selection for series-expanded, residual-stress inverse solutions. J. Eng. Mater. Technol. 128 (2), 175–185. http://dx.doi.org/10.1115/1.2172278, URL: https://asmedigitalcollection.asme.org/materialstechnology/article/128/2/175/464917/Uncertainty-Model-Error-and-Order-Selection-for.

Rice, J.R., 1972. Some remarks on elastic crack-tip stress fields. Int. J. Solids Struct. 8 (6), 751–758. http://dx.doi.org/10.1016/0020-7683(72)90040-6, URL: https://linkinghub.elsevier.com/retrieve/pii/0020768372900406.

Rosenthal, I., Shneck, R., Stern, A., 2018. Heat treatment effect on the mechanical properties and fracture mechanism in AlSi10Mg fabricated by additive manufacturing selective laser melting process. Mater. Sci. Eng. A 729, 310–322. http://dx.doi.org/10.1016/j.msea.2018.05.074, Publisher: Elsevier.

Salmi, A., Atzeni, E., 2017. History of residual stresses during the production phases of AlSi10Mg parts processed by powder bed additive manufacturing technology. Virtual Phys. Prototyp. 12 (2), 153–160. http://dx.doi.org/10.1080/17452759.2017.1310439, URL: https://www.tandfonline.com/doi/full/10.1080/17452759.2017.1310439.

Salmi, A., Atzeni, E., Iuliano, L., Galati, M., 2017. Experimental analysis of residual stresses on AlSi10Mg parts produced by means of selective laser melting (SLM). Procedia CIRP 62, 458–463. http://dx.doi.org/10.1016/j.procir.2016.06.030, URL: https://linkinghub.elsevier.com/retrieve/pii/S2212827116306485.

Savitzky, A., Golay, M.J.E., 1964. Smoothing and differentiation of data by simplified least squares procedures. Anal. Chem. 36 (8), 1627–1639. http://dx.doi.org/10.1021/ac60214a047, URL: https://pubs.acs.org/doi/abs/10.1021/ac60214a047.

Schajer, G.S., Prime, M.B., 2006. Use of inverse solutions for residual stress measurements. J. Eng. Mater. Technol. 128 (3), 375. http://dx.doi.org/10.1115/1.2204952, URL: http://MaterialsTechnology.asmedigitalcollection.asme.org/article.aspx?articleid=1427760.

Schindler, H.J., 1996. Determination of residual stress distributions from measured stress intensity factors. Int. J. Fract. 74 (2), R23–R30. http://dx.doi.org/10.1007/BF00036266, URL: http://link.springer.com/10.1007/BF00036266.

Schindler, H.J., Bertschinger, P., 1997. Some steps towards automation of the crack compliance method to measure residual stress distributions. In: Proceedings of the 5th International Conference on Residual Stress. pp. 682–687.

Schindler, H.J., Cheng, W., Finnie, I., 1997. Experimental determination of stress intensity factors due to residual stresses. Exp. Mech. 37 (3), 272–277. http://dx.doi.org/10.1007/BF02317418, URL: http://link.springer.com/10.1007/BF02317418.

Shiomi, M., Osakada, K., Nakamura, K., Yamashita, T., Abe, F., 2004. Residual stress within metallic model made by selective laser melting process. CIRP Ann. 53 (1), 195–198. http://dx.doi.org/10.1016/S0007-8506(07)60677-5, URL: https://linkinghub.elsevier.com/retrieve/pii/S0007850607606775.

Strantza, M., Vrancken, B., Prime, M., Truman, C., Rombouts, M., Brown, D., Guillaume, P., Van Hemelrijck, D., 2019. Directional and oscillating residual stress on the mesoscale in additively manufactured Ti-6Al-4V. Acta Mater. 168, 299–308. http://dx.doi.org/10.1016/j.actamat.2019.01.050, URL: https://linkinghub.elsevier.com/retrieve/pii/S1359645419300655.

Tsai, S.-D., Mahulikar, D., Marcus, H., Noyan, I.C., Cohen, J., 1981. Residual stress measurements on Al-graphite composites using X-ray diffraction. Mater. Sci. Eng. 47 (2), 145–149. http://dx.doi.org/10.1016/0025-5416(81)90220-2, URL: https://linkinghub.elsevier.com/retrieve/pii/0025541681902202.

Vaidyanathan, S., Finnie, I., 1971. Determination of residual stresses from stress intensity factor measurements. J. Basic Eng. 93 (2), 242–246. http://dx.doi.org/10.1115/1.3425220, URL: https://asmedigitalcollection.asme.org/fluidsengineering/article/93/2/242/439812/Determination-of-Residual-Stresses-From-Stress.

Vrancken, B., 2016. Study of Residual Stresses in Selective Laser Melting (Ph.D. thesis). KU Leuven.

Vrancken, B., Wauthlé, R., Kruth, J.-P., Van Humbeeck, J., 2013. Study of the influence of material properties on residual stress in selective laser melting. In: 2013 International Solid Freeform Fabrication Symposium. University of Texas at Austin.

Williams, R.J., Hooper, P.A., Davies, C.M., 2018. Finite element prediction and validation of residual stress profiles in 316L samples manufactured by laser powder bed fusion. Procedia Struct. Integr. 13, 1353–1358. http://dx.doi.org/10.1016/j.prostr.2018.12.283, URL: https://linkinghub.elsevier.com/retrieve/pii/S2452321618305213.

Wohlers, T., Campbell, R.I., Diegel, O., Huff, R., Kowen, J., 2020. Wohlers Report 2020: 3D Printing and Additive Manufacturing State of the Industry. OCLC: 1200744602.

Wu, J., Wang, L., An, X., 2017. Numerical analysis of residual stress evolution of AlSi10Mg manufactured by selective laser melting. Optik 137, 65–78. http://dx.doi.org/10.1016/j.ijleo.2017.02.060, URL: https://linkinghub.elsevier.com/retrieve/pii/S0030402617302036.

Yu, W., Sing, S.L., Chua, C.K., Tian, X., 2019. Influence of re-melting on surface roughness and porosity of AlSi10Mg parts fabricated by selective laser melting. J. Alloys Compd. 792, 574–581. http://dx.doi.org/10.1016/j.jallcom.2019.04.017, URL: https://linkinghub.elsevier.com/retrieve/pii/S0925838819312812.

Zhang, W., Tong, M., Harrison, N.M., 2020. Scanning strategies effect on temperature, residual stress and deformation by multi-laser beam powder bed fusion manufacturing. Addit. Manuf. 36, 101507. http://dx.doi.org/10.1016/j.addma.2020.101507, URL: https://linkinghub.elsevier.com/retrieve/pii/S2214860420308794.

Zienkiewicz, O.C., Taylor, R.L., Zhu, J.Z., 2013. The Finite Element Method: Its Basis and Fundamentals, seventh ed. Elsevier, Butterworth-Heinemann, Amsterdam, OCLC: ocn852808496.